Research in Astronomy and Astrophysics, 22:115014 (14pp), 2022 November https://doi.org/10.1088/1674-4527/ac92f8

Investigation of Mode Changing, Pulse Nulling and Subpulse Drifting Properties in the Asymmetric Conal Triple Radio Pulsar B2319+60

Jian-Ling Chen[1], Zhi-Gang Wen[2,3,4,5], Hong-Guang Wang[2,6], Na Wang[2], Rai Yuen[2], Vishal Gajjar[7], Jian-Ping Yuan[2], Zhen Wang[2,8], Wen-Ming Yan[2], Jin-Peng Wang[1], Cheng-Bing Lyu[6], Hui Wang[1], and Xue-Feng Duan[2,4]
[1] Department of Physics and Electronic Engineering, Yuncheng University, Yuncheng 044000, China
[2] Xinjiang Astronomical Observatory, Chinese Academy of Sciences, Urumqi 830011, China; wenzhigang@xao.ac.cn
[3] Key Laboratory of Radio Astronomy, Chinese Academy of Sciences, Nanjing 210008, China
[4] Key Laboratory of Microwave Technology, Urumqi 830011, China
[5] Guizhou Provincial Key Laboratory of Radio Astronomy and Data Processing, Guiyang 550001, China
[6] Center for Astrophysics, Guangzhou University, Guangzhou 510006, China
[7] Space Science Laboratory, University of California, Berkeley 94710, United States of America
[8] School of Physical Science and Technology, Xinjiang University, Urumqi 830046, China
Received 2022 July 20; revised 2022 September 1; accepted 2022 September 15; published 2022 November 2

Abstract

We report on a detailed analysis of the mode changing, nulling and subpulse drifting behavior of the conal triple pulsar B2319+60 at 1.5 GHz observed with the Nanshan 25 m radio telescope. The pulsar's profile can be interpreted as resulting from a sightline traverse which cuts across an outer cone and tangentially grazes an inner cone. About 30 per cent of nulls are found to create alternating bunches of nulls and emission in a quasi-periodic manner with an averaged fluctuation rate of about four rotation periods (P_1). The presence of two distinct drift modes (A and ABN) plus a phase-stationary non-drift emission mode (B) is confirmed, and each corresponds to a different pulse profile. The mode A is dominated by a phase modulation in the trailing component with a circulation time of around $7P_1$. In addition to a $3P_1$ phase modulation in the leading component, mode ABN presents an amplitude modulation in the leading and trailing components with a period of around $40P_1$. The emission region and geometry remain constant during mode changing. The diversity seen in the individual pulse behavior of the pulsar B2319+60 provides a unique window into the emission physics.

Key words: (stars:) pulsars: general – (stars:) pulsars: individual (PSR B2319+60) – stars: neutron

1. Introduction

Pulsars are famous as precise clocks in areas of fundamental physics, which are attributed to their exceptionally regular rotations and stable integrated pulse profiles. The integrated pulse profiles constituted by averaging over tens of thousands of periods become highly stable for the majority of pulsars, and remain stable over at least years. In most cases, the pulsed emission from every single rotation (thus individual or single pulse) is extremely variable in intensity, phase, shape and polarization. Nevertheless, some peculiar pulsars exhibit various temporal variations in pulse profile, showing no detectable emission for a period of time (pulse nulling) (Backer 1970c), switching between two or more additional stable patterns of integrated profiles (mode switching or changing) (Backer 1970b), or manifesting systematic subpulse drift motion through the pulse window (subpulse drifting) (Drake & Craft 1968). The transitions between burst and null states are very rapid, usually within one rotation period, but nulling durations vary, ranging from a few periods to hours (Wen et al. 2016b).

Pulsar B2319+60 is a representative old and slow radio pulsar with a rotational period (P_1) of 2.256 s and a spin-down age (τ_c) of 5 Myr. It is among the few pulsars exhibiting multiple distinct and reproducible drift modes whose single pulse sequence (hereafter PS) behavior was investigated at 1415 MHz by Wright & Fowler (1981). When not in a null state, the pulsar switches between three distinct modes of radio emission labeled A, B and ABN (a nomenclature that will also be used here for continuity), each corresponding to a different subpulse drift rate and integrating into a different pulse profile. Such correlation between pulse profile and subpulse drift rate is also present in some other pulsars (e.g., PSRs B1918+19, B2303+30) (Redman et al. 2005; Rankin et al. 2013). Transitions between these modes were found to interact in specific sequences. The drift feature and modes were also identified by Weltevrede et al. (2006, 2007), and classified as a coherent drifter.

The radio emission from pulsars originates from the plasma process in the highly magnetized magnetosphere. The emission mechanism is still not clearly understood. The phase modulated subpulse drifting can be explained as the $\boldsymbol{E} \times \boldsymbol{B}$ drift in the inner acceleration gap, and this is the only known source of periodicity in single pulse dynamics. However, the periodic-nulling and amplitude modulation phenomena are difficult to be explained (Basu & Mitra 2018). The nulling and mode switching are proposed to be associated with emission

beam geometric reconfiguration or current redistribution (Timokhin 2010). However, the trigger mechanism remains a mystery. The pulsar emission physics could be informed from the morphological characteristics of observed pulse waveforms. The average profile represents the elemental stationary property of pulsar emission, whereas an individual PS manifests ordered or stochastic processes. The hybrid understanding of both will develop the physical basis in the emission region straightforwardly. In this paper, we analyze this pulsar's drift modulation, nulls, profile pattern and polarization more thoroughly based on observations carried out by the Nanshan radio telescope. The huge volumes of data will facilitate a proper characterization of the emission properties.

In Section 2, we describe the radio observations and data reduction of PSR B2319+60. In Section 3, we present the mean pulse profile and polarimetric characteristics, which will be referenced to infer the pulsar's basic emission geometry. Section 4 presents the multiple features in single PSs, including nulling, mode changing and subpulse drifting. Section 5 discusses the emission geometry and the association between subpulse drifting and mode changing. Finally, conclusions are given in Section 6.

2. Observations and Data Reduction

The extensive data were collected from long-term timing, successive single-pulse, polarization and mode changing programs carried out with the Nanshan 25 m radio telescope located in Xinjiang, China. The cryogenic receiver system consists of twin channel pre-amplifiers, which is used to receive orthogonal linear polarizations in the band 1380−1700 MHz. The unpolarized quasar 3C295 was adopted as calibrator with a fixed flux density of 14.818 Jy in the frequency band, giving an equivalent system flux density on cold sky of approximately 198.819 Jy. Polarimetric and flux calibration were achieved using a semiconductor diode, which was controlled periodically to inject linearly polarized pulsed noise into the feed horn at 45° to the dual-channel probes. The signals were then amplified and down-converted to an intermediate frequency. After conversion, the signals were fed to one of the two data acquisition systems separately in incoherent filterbank mode.

The analog filterbank system (AFB), having a total bandwidth of 320 MHz centered at 1540 MHz with 128 2.5 MHz channels on each of two orthogonal linear polarizations, was used for both search and fold mode observations (Wang et al. 2001). The detected power in each channel was digitized in 1 bit every 1 ms before being written to an output buffer. The data were then acquired using a data acquisition card and recorded to a hard disk drive for off-line processing. The AFB also provided a flexible system for reducing the data volume and achieving high signal-to-noise ratio (S/N). The data from each frequency channel were folded at the apparent pulsar period to form subintegrations of typical duration around 1 minute. The calibrated observations were provided by a digital filterbank system (DFB) with a frequency resolution of 0.5 MHz, or 1024 channels across the full band (Wen et al. 2016a). The full-Stokes spectra were acquired in a 512 MHz bandwidth centered at 1556 MHz radio frequency. The bandpass rolled off at the edges of the observing frequency with the limited receiver bandwidth. The DFB yielded 8-bit Nyquist-sampled data, with synchronous folding on-line at the pulsar period accumulated every 30 s. The summary of our observations used for analysis of the emission properties is listed in Table 1.

Table 1
Summary of Radio Observations of PSR B2319+60 for Analysis of the Emission Properties

Date (yyyy-mm-dd)	Backend	Mode	Duration (hr)	Calibration (Y/N)
2011-01-01	AFB	Fold	3.00	N
2011-01-06	AFB	Fold	3.00	N
2012-03-28	DFB	Fold	4.25	N
2012-04-29	DFB	Fold	5.90	N
2013-01-30	AFB	Fold	0.96	N
2013-03-24	AFB	Search	5.99	N
2013-04-05	AFB	Search	12.00	N
2014-02-25	AFB	Fold	2.00	N
2016-06-17	AFB	Search	1.06	N
2017-07-26	DFB	Fold	20.25	Y
2017-08-07	DFB	Fold	7.46	Y

In the off-line data reduction, the search-mode data sets are processed using the DSPSR software package (van Straten et al. 2010), which subdivides the data into single-pulse time series with 512 phase bins across the pulse period. For fold-mode observations, the data are processed with the PSRCHIVE software package (Hotan et al. 2004). The routine PAZ is utilized to remove the vast majority of spurious radio frequency interference (RFI) signals by employing the median difference filter. Additionally, 5% of each band edge is excised as well. Subsequently, we flux and polarization calibrate observations using the PAC routine (van Straten et al. 2012). The flux calibrations are applied from solutions obtained via observations of 3C295. The gains and phases are corrected from the constructed polarization calibration solutions. Finally, the data are incoherently dedispersed at the cataloged dispersion measure (DM) of 94.591 pc cm^{-3} (Manchester et al. 2005) to remove sub-channel dispersive smearing and averaged across all frequency channels. The rotation measure (RM) was obtained by a brute-force search for peak linear polarization and then iterative refinement of differential position angle. The RM was measured to be -231.8 ± 0.9 rad m^{-2} for Faraday rotation correction, which is consistent with the value of -232.6 ± 0.2 rad m^{-2} given by Force et al. (2015). A two-dimensional pulse stack is produced with one axis along the

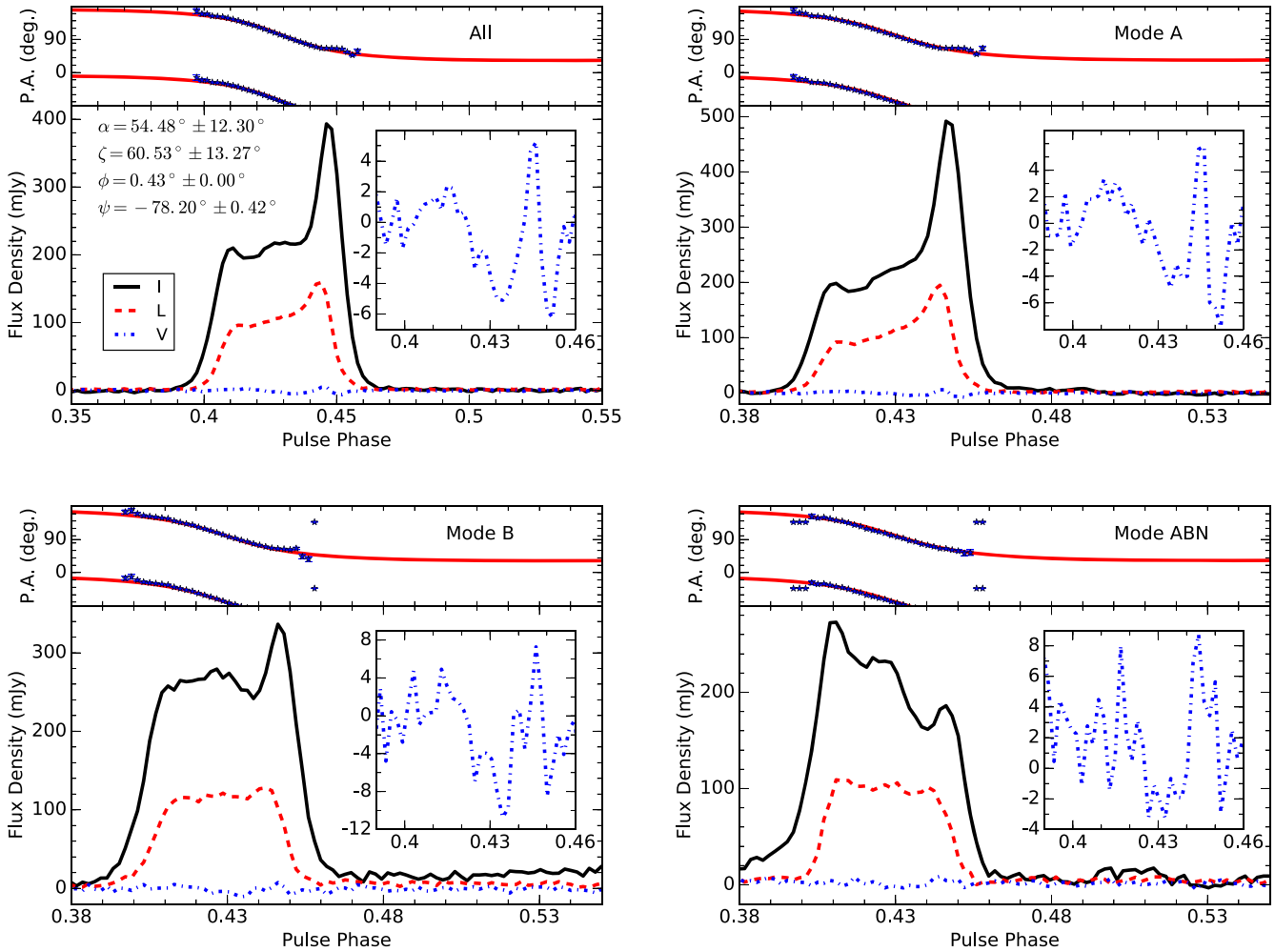

Figure 1. Polarimetric average profiles of PSR B2319+60 computed from two long DFB calibrated observations. The lower panels give the total intensity (Stokes I, solid curve), the total linear (Stokes $L = \sqrt{(Q^2 + U^2)}$, dashed red) and the circular polarization (Stokes V, dash–dotted blue). The inset is an expanded version of small amounts of circular polarization. The upper panels present the measured PPA $= \frac{1}{2}\tan^{-1}(U/Q)$ traverse, as well as a fitted curve computed based on the rotating-vector model (RVM). The fitted parameter values at the upper left of the lower panel: magnetic latitude α, sightline circle radius ζ, central longitude ϕ and fiducial PPA ψ. The segregated polarimetric mean profiles for three modes are presented as well. Each mode is summed from the number of subintegrations indicated.

pulse longitude, and the other along the pulse number. Further analyses for measuring subpulse drifting features and identifying emission modes and nulling are carried out on the PSs.

3. Polarimetric Pulse Profile

In order to obtain accurate values of total intensity and average polarization, two long DFB calibrated observations are aligned and averaged in time using the timing ephemeris. Summing observations over different epochs does not significantly affect the polarization pulse profiles (Ng et al. 2020). The measurements of polarization profile and geometric position angle (hereafter PPA) variation (upper left plot in Figure 1) are fundamental in providing a basis for understanding the beaming of radio emission. The total power, and linear and circular polarization of the profile are given in the lower panels. The PPA information is presented in the upper panels and only used when the linear polarization exceeds three times the standard deviation as observed in the off-pulse region. The highly asymmetric total intensity consists essentially of three overlapping components. The leading and central components are of nearly equal height, and the trailing component is dominant and roughly double the others. The mean flux density is measured to be 12.54 ± 0.02 mJy.

The pulsar is moderately linearly polarized (dashed red curve in the lower panel of the upper left plot of Figure 1), with higher fractional linear polarization in the trailing component. The aggregate circular polarization V (dash–dotted blue curve in the lower panel of the upper left plot of Figure 1) never exceeds about 1.5%. The sense reverses from left-hand to right-

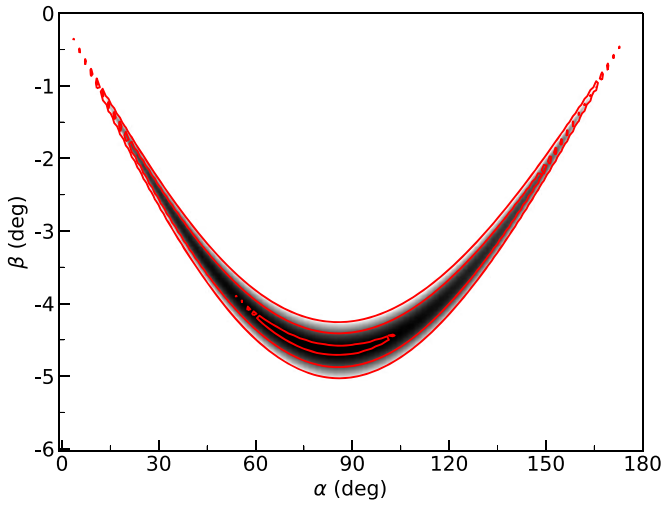

Figure 2. The results of fitting an RVM curve for each (α, β) combination. The reduced chi-square (χ^2) of the fit is shown as the gray scale, with the darkest value corresponding to the best fit. Evidently, α and β are highly correlated. The red contour lines represent 1σ, 2σ and 3σ confidence boundaries.

hand under the leading part of the profile, and conversely under the trailing part. The PPA follows the classic "S-shaped" excursion across the pulse with a total traverse of about 120° (shown in the upper panel of the upper left plot of Figure 1). The PPA traverse can be well fitted using the RVM (Radhakrishnan & Cooke 1969). The fitted parameter values are presented at the upper left of the lower panel: the central longitude ϕ and PPA at the central longitude ψ as well as the magnetic latitude α and the sightline circle radius $\zeta = \alpha + \beta$, where β corresponds to the sightline impact angle. As is shown, the quantities ϕ and ψ are significantly constrained. However, the α and β values obtained from the fit are extremely covariant and unreliable due to the limited duty cycle of the profile (Mitra & Li 2004; Wen et al. 2020). Figure 2 shows the reduced χ^2 values of the fit as a function of α and β. Evidently, there are a number of combinations of α and β that provide equally acceptable fits. Therefore, the actual geometry of the system cannot be necessarily represented by the derived angles. From the RVM fit alone, we can conclude that $-5° < \beta < -1°$, corresponding to a negative gradient of the position angle swing. Nevertheless, the fact is that α is practically unconstrained. Using the empirical theory of pulsar emission, the geometry of PSR B2319+60 is estimated to be $\alpha \sim 18°$ and $\beta \sim -2.°4$ (Rahaman et al. 2021), which falls within our confidence interval.

4. Pulse Sequence Modulation

Single pulses preserve concrete information on the pulsar radio emission and propagation in the magnetosphere from every single rotation, the investigation of which can shed light

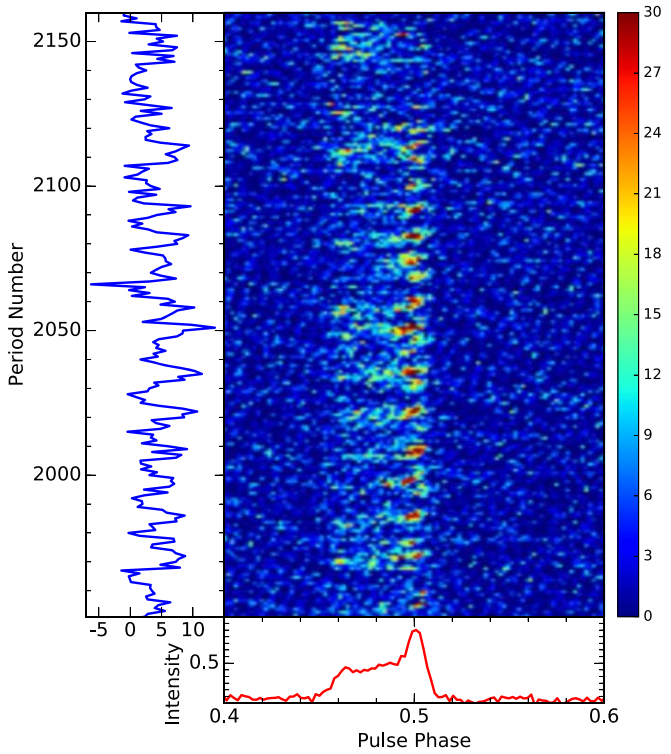

Figure 3. The top panel shows a section of 200 consecutive individual pulses for PSR B2319+60 observed at 1540 MHz from Nanshan radio telescope, while the bottom panel displays the profile integrated by the above pulses. Time runs left to right across the pulse window (pulse phase) and bottom to top with period number. The subpulse drifting is visible in the trailing component, and interrupted by short nulls. The left panel depicts the energy sequence averaged by all the phase bins inside the on-pulse window.

on the nature of the pulsar emission mechanism. An extract from our longest search mode observations presented in Figure 3 shows the essential features of B2319+60's single pulse behavior. The pulses with no detectable emission are clearly visible between pulse numbers 1960–1970 and 2130–2140. It should be noted that the profile switches to another pattern with a prominent leading component from pulse numbers 2142 to 2158 and 2110 to 2120. The prominent drift bands are clearly apparent in the trailing component, but not present in the leading and central components by visual inspection.

4.1. Nulling Behavior

Usually, interstellar scintillation is responsible for the intensity fluctuation in time and frequency domains on a large scale. The scintillation bandwidth at 1540 MHz is expected to be 0.05 MHz which is much smaller than the observing bandwidth of 400 MHz according to the NE2001 Galactic free electron density model (Cordes & Lazio 2002). Therefore, the effect of the intensity fluctuations caused by scintillation is

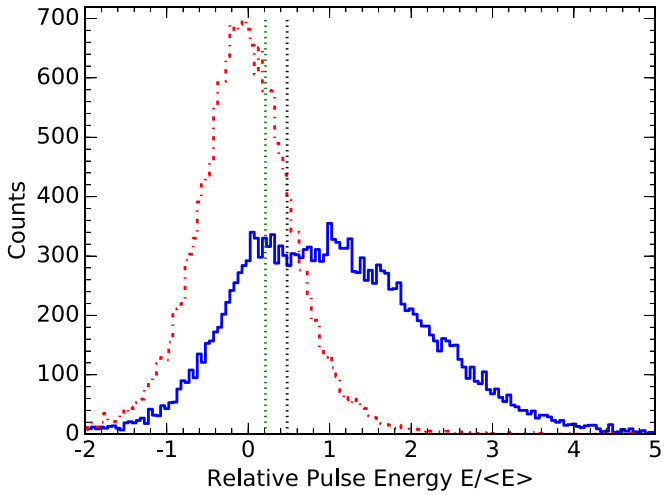

Figure 4. Relative on-pulse energy histogram (solid curve) for the long observation of B2319+60 and a corresponding off-pulse noise window (dash–dotted curve) is scintillation correction as explained in the text. The NF was estimated to be $35.73 \pm 0.43\%$, which gives a high threshold at the point where null and burst pulse distributions cross each other (around 0.48 $E/<E>$) in the on-pulse histogram (black dotted vertical line). The green dotted vertical line is selected lower threshold (around 0.21 $E/<E>$) at the energy where nulls and bursts are separated.

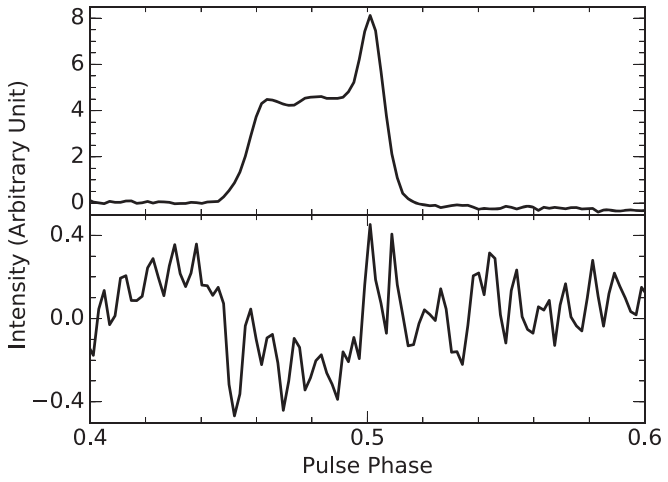

Figure 5. The integrated pulse profiles obtained from the separated nulls (bottom panel) and bursts (top panel). The null profile does not show any detectable profile component with significance above 3σ, which suggests the absence of any weak level emission.

invisible in frequency. In order to eliminate the intensity fluctuation in time, the pulse energies are addressed by comparing with a running average of 1300 pulse energies (which is equivalent to the scintillation timescale) instead of simply averaging pulse energy from the whole observation. The pulse energies are subtracted by a running mean value of the length of the scintillation timescale.

Figure 4 presents the scintillation-corrected and normalized energy distributions for the on-pulse windows and off-pulse windows, which provide statistical information for the characterization of pulse nulling properties. The histogram formed from off-pulse energies (dash-dotted line) is centered around zero, which represents the Gaussian random noise contributed by the system temperature. The null pulse distribution and the burst pulse distribution are not very distinguishable in the on-pulse energy histogram (solid line). The nulling fraction (NF) is estimated to be around $35.73 \pm 0.43\%$ by subtracting a scaled version of the off-pulse histogram from the on-pulse histogram at zero energy. The procedure is similar to that used for detecting pulse nulling from the single PSs by Wang et al. (2007), Wen et al. (2016b). The obtained NF is overestimated compared with 29 ± 1 reported by Gajjar et al. (2012), which is due to the mixing between the null pulses and the low S/N burst pulses. In order to get a well-defined bimodal distribution, a range of consecutive pulses from 2 to 50 is subintegrated. The bimodal distribution of on-pulse energy can be obtained by subintegrating 20 consecutive pulses, which gives the estimation of NF to be around 29.68 ± 0.94.

In order to carry out further analysis, a similar procedure presented by Gajjar et al. (2014) is adopted to identify burst and null pulses. All the single pulses are arranged in the ascending order of their on-pulse energy. Null pulses are tagged with on-pulse energy below the threshold which is determined through the estimated NF (dotted vertical line in Figure 4). However, the burst pulses with low energy are tagged as nulls as well using the threshold, because the histograms of bursts and nulls are not well separated. To identify these low-energy burst pulses among nulls, the pulses are removed from the high-energy end until the remaining integrated null pulse profile shows no emission with significance above 3σ. Then a conservative threshold is determined with lower energy around 0.21 $E/<E>$. The individual pulses below such threshold are classified as null pulses, while the remaining are burst pulses. The indicated threshold gives an estimation for the lower limit on the NF to be $27.06\% \pm 0.38\%$. Figure 5 presents the integrated pulse profiles obtained from all separated bursts (top panel) and nulls (bottom panel). There is no obvious energy with S/N larger than 3 in the null pulse profile.

Usually, a nulling pulsar switches between null and burst states with various timescales, which provides an important clue to scrutinize various nulling mechanism models. In order to estimate the distribution of null and burst durations, the null lengths and burst lengths are measured. Figure 6 displays the obtained null length and burst length histograms. The non-random distribution shows an power-law slope with relatively higher number of short null and burst lengths, which is consistent with the results reported by Gajjar et al. (2012). The extremely short nulls are also obvious in the PS (Figure 3), which interrupt the burst bunches. The average null length is around two periods. The burst lengths on the other are of much

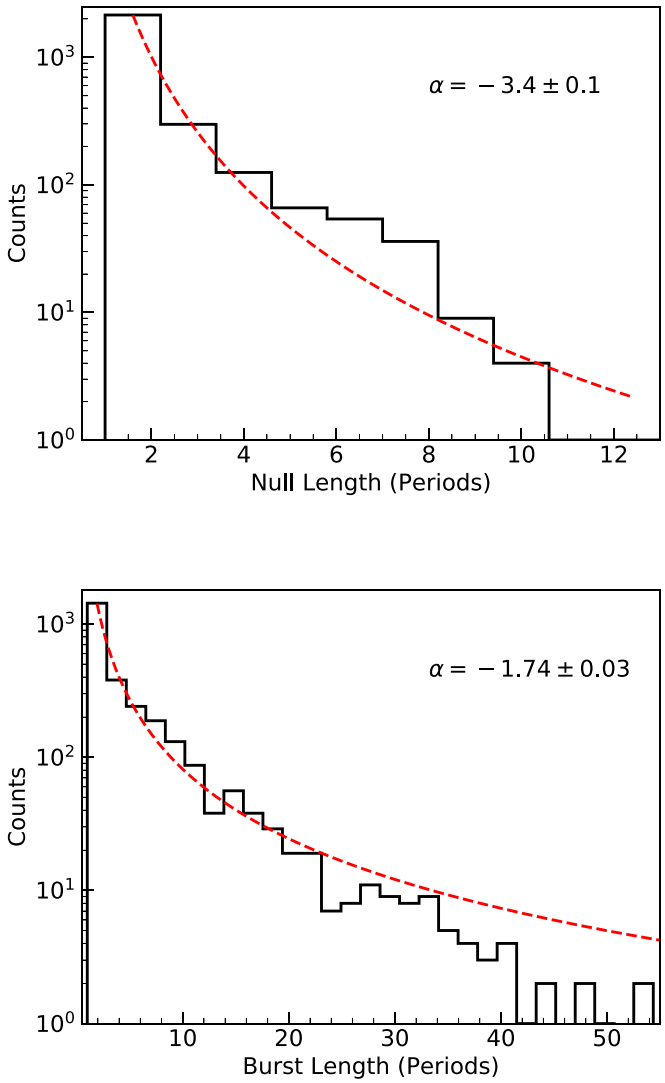

Figure 6. The observed histograms of null length (top) and the burst length (bottom). There is a clear power-law decay in the frequency of occurrence from shorter durations to longer durations in both histograms. The best-fit power-law distributions for both histograms are overdrawn. The longest burst length is 93 periods, which is outside the scope of the histogram.

longer durations, reaching a maximum of around 93 consecutive periods and an average length of around five periods.

Previous studies indicated that nulling may not be random (Herfindal & Rankin 2007). In order to investigate whether PSR B2319+60 presents quasi-periodic switch between the null and burst states, all the burst pulses are marked as ones and all remaining pulses (nulls) are marked as zeros. Then a fast Fourier transform (FFT) is calculated on the formed time series of binary numbers. An FFT length of 256 periods at a time is carried out to estimate the nulling periodicity. The starting period is shifted by ten periods and the process is repeated until the end of the observations to determine the temporal evolution in the nulling periodicity. Figure 7 presents the spectrum with a

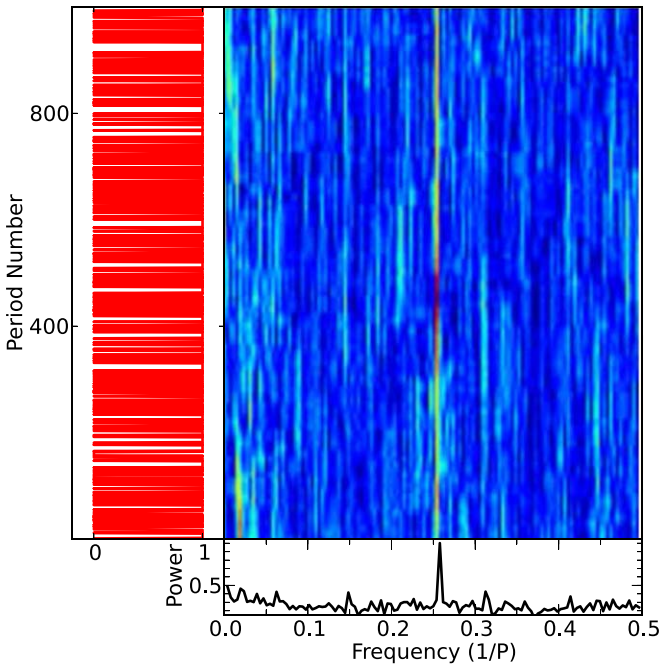

Figure 7. Quasi-periodic fluctuations in the pulse energy of PSR B2319+60 at 1540 MHz. The main panel shows a zoomed in (along x-axis) FFT for the null/burst sequence where the nulls have been replaced with "0" and bursts with "1" (left panel). The time averaged FFT is presented in the lower panel. A clear strong periodicity of 3.8 ± 0.1 periods is indicated in the Fourier spectrum of the pulse energy modulation pattern using an FFT length of 256 periods at a time.

clear quasi-periodic feature around 3.8 ± 0.1 periods, where the uncertainty is estimated from the full width at half maximum of the spectrum. Such non-randomness is also obvious from the massive excess of burst bunches at four pulse periods in the null length and burst length histograms depicted in Figure 6.

4.2. Subpulse Drifting Patterns

In order to characterize the subpulse modulation whether in a systematic or a disordered fashion, the longitude-resolved fluctuation power spectrum (hereafter LRFS, displayed in Figure 8) is carried out (Backer 1970a). The interruption of quasi-periodic nulls in the burst bunches may smear out the drift features, which results in a challenging task in the measurement of the drifting features. Therefore, the identified nulls are removed from the single PS, which results in an artificial sequence with only burst pulses. The newly formed PS is then separated into blocks with a fixed length of 512 pulses. The LRFS on each block is computed by performing a discrete Fourier transform over each individual phase bin. The final spectrum is obtained by averaging the fluctuation power spectra of the different blocks. A 512-point FFT is set to achieve a relatively high frequency resolution. A red noise component which increases in strength with decreasing fluctuation frequency is attributed to interstellar scintillation, slow modulation intrinsic to the pulsar emission, and/or possible slow

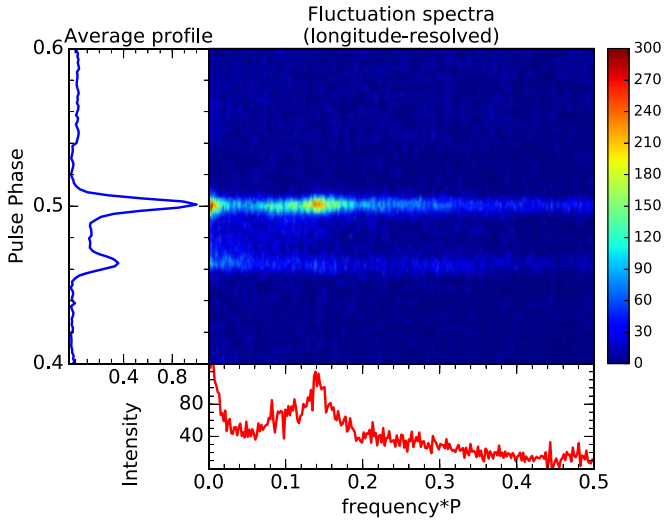

Figure 8. LRFS (main panel, per the color scale at the right). The units of the horizontal axis are in cpp, which corresponds to P_1/P_3 in the case of drifting (where P_1 is the pulsar rotational period, and P_3 is the interval over which the subpulses repeat at any specific location within the pulse window). The vertical axis is the pulse phase in degrees. A 512-point FFT is used and averaged over the blocks of PS with null pulses removed. The total power profile is plotted and aligned with the LRFS in the left-hand panel, and the integral spectrum from the on-pulse window is given at the bottom of the figure. Note that a distinct feature in the trailing component with excess of power is clearly visible in the integral spectrum.

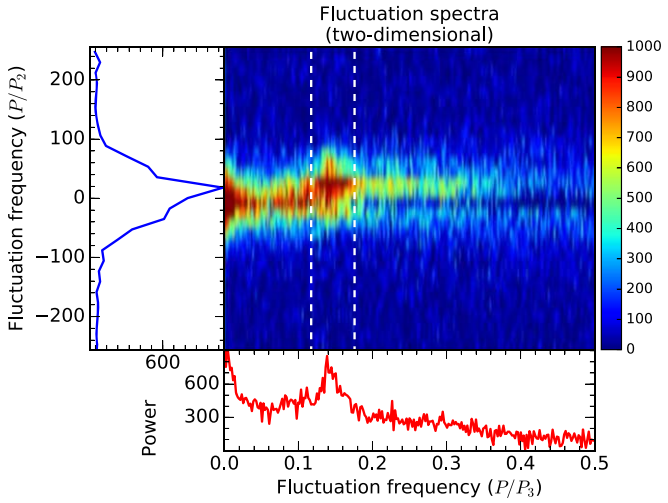

Figure 9. Two-dimensional fluctuation power spectrum (main panel, per the color scale at the right) for the same PS as in Figure 8. The horizontal axis has the same units as the LRFS, but the units of the vertical axis are also cpp, which correspond to P_1/P_2 in the case of drifting (where P_2 is the longitudinal separation between two adjacent drift bands in degrees). The left panel shows the horizontal integrations of power between the dashed lines. The vertical integration gives the power spectrum in the bottom panel.

variations in the instrumental gain. Given that our 2.5 MHz bandwidth is larger than the decorrelation bandwidth, we do not expect scintillation to affect our spectra. A distinct region of the LRFS with excess of power is confined narrowly in the phase of the trailing component, which indicates that the pulsar is modulated at frequency around 0.14 cycles per period (cpp) or a cycle of nearly seven periods.

Although the LRFS is a sensitive method to determine the time-averaged properties of periodic subpulse modulation, it is still in a state of uncertainty whether the above determined modulation originated from intensity or phase variation. In order to turn uncertainty into reality, the two-dimensional fluctuation spectrum (hereafter 2DFS) is calculated in Figure 9 (Edwards & Stappers 2002). As we can see, an evident drift feature associated with the trailing component is presented at the same frequency as in the LRFS, and is offset from the horizontal axis by $P_2 \simeq P_1/18 = 0.056P_1$, in addition to a prominent red noise fluctuation with extremely low frequency. The detected periodicity is the most common drift feature found by Wright & Fowler (1981), and is common with the results conducted with Westerbork Synthesis Radio Telescope (WSRT) observations at 21 cm and 92 cm (Weltevrede et al. 2006, 2007).

4.3. Distinguishing the Modes

Modal effects are among the most fascinating and important behavior in PSR B2319+60, which is reported to consist of three averaged pulse profiles (Wright & Fowler 1981). The polarimetric average pulse profiles of modes A, B and ABN are shown in Figure 1. Modes A and ABN are easily distinguished according to their evident difference in the peak density ratio between the leading and trailing components. The ABN mode is recognized as structure of the pronounced leading component, and reduced energy in turn for the central and trailing components. The A and B modes have very similar mean pulse profiles, differing slightly in the integrated energy of their leading and central components. Mode B is much brighter than modes A and ABN in average flux density. In order to distinguish the profile modes quantitatively, the artificial PSs with nulls marked are investigated. The peak intensity ratio of the leading to the trailing components is used as an indicator for the potential mode ABN. The distribution of the peak intensity ratio is shown in the left plot of Figure 10, which extends over a wide ratio range. Following the method described by Wen et al. (2016a), a model that combines two Gaussian components is adopted to discriminate mode ABN from modes A and B by least-squares fitting the ratio distribution. The intersection of the two Gaussian curves is adopted as the threshold and the pulses with peak intensity ratio larger than 0.76 are identified as mode ABN, while the remaining pulses are classified as modes A and B. The distribution of mode ABN is wider than those of modes A and B, which suggests that mode ABN is more unstable than modes A and B. To distinguish modes A and B from the PSs with nulls erased and mode ABN marked, the flux density ratio of the leading and central components to the trailing component is

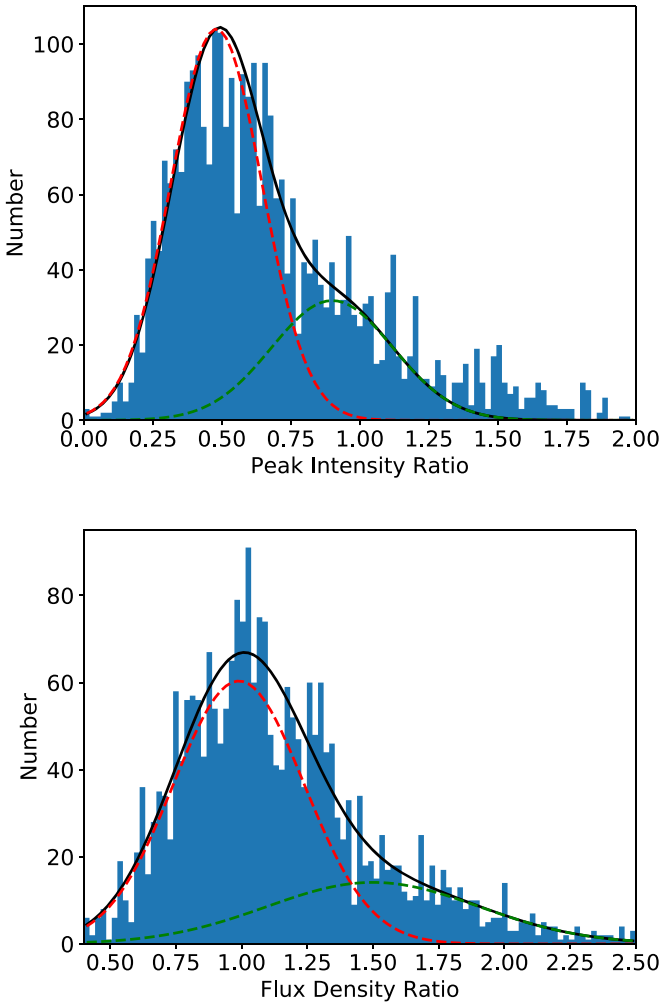

Figure 10. Left: histogram of the peak intensity ratio of the leading component to the trailing component. Right: histogram of the flux density ratio of the leading and central components to the trailing component. The black solid line represents the fitting based on the combination of two Gaussian components (dashed red and dashed green lines).

calculated for each pulse. The histogram of the flux density ratio is shown in the right plot of Figure 10, which also presents an extension of the wide ratio range. Therefore, a combination of two Gaussian components corresponding to modes A and B is used to fit the ratio distribution. Likewise, the intersection of the two Gaussian curves is taken as the threshold. The pulsar is identified in mode A with ratio less than 1.42, and the remainder is labeled as mode B. The distribution of mode A is considerably narrower than that of mode B, which indicates that mode A is more stable than mode B.

The results of the stacked subintegrations and separated profile modes are obviously indicated in Figures 11 and 12 based on the profile diversity. In the majority of the PSs the modes can be identified on the basis of the above method. However, in some instances it proves difficult either due to mixing of the modes or reduction in intensity. Among all the 65 hr of data, 757 mode A, 650 mode B and 506 mode ABN sequences are identified. The total durations of modes A, B and ABN are calculated to be about 52.18%, 23.85% and 17.47%, respectively. Compared with the previous results, the enlarged occupation ratios resulted from the combination of burst pulses and neighboring few nulls. The pulsar transitions frequently between three burst modes and nulling state.

Figure 13 presents the histograms of the duration of three modes. The occurrence of the modes decreases at longer timescales. The most prevalent emission mode A is sustained over longer intervals, occasionally lasting as long as 20 minutes (530 pulses). Modes B and ABN have similar timescale distributions with much shorter durations than that of mode A, which suggests that mode A is more stable than modes B and ABN.

4.4. Mode-resolved Fluctuation Spectra

As suggested by Wright & Fowler (1981), every pulse profile corresponds to a distinct drift pattern. Although a significant drift pattern is detected and measured in PSR B2319 +60, it is still a challenging task to identify the drift properties for the three modes accurately. Based on the mode's identification technique, the individual pulses can be separated out from the PSs. Then three artificial PSs corresponding to modes A, B and ABN are formed for the mode dependent modulation study. Figures 14, 15 and 16 give the LRFSs and 2DFSs of modes A, B and ABN, respectively. We have measured the drifting features in three sequences where a clear frequency peak could be identified as reported in Table 2. The modulation feature of mode A resembles that of total observations with a periodicity of $7.4 \pm 1.2P_1$ and a positive drift sense $P_2 = 20^{\circ}.1 \pm 7^{\circ}.5$. In contrast, no clear drifting peak is seen in mode B, which indicates disordered subpulse motion during this mode. However, a widish structure can be discerned at $P_3 = 3.1 \pm 0.7P_1$, mainly appearing in the leading component for mode ABN. The low-frequency excess power is also present at $P_3 = 40P_1$ in the leading and trailing components, which could be related to nulling or mode changes. Furthermore, they are not harmonically related to each other. The detected subpulse drifting features are seen primarily in the leading and trailing components with no signatures visible in the central component, which suggests that drifting is restricted to the outer conal regions.

Wright & Fowler (1981) demonstrated that the multiple drift modes from pulsar B2319+60 occurred in sequences of increasing drift rate. More specifically, it exhibits three characteristic modal sequence patterns: $\mathrm{A} \rightarrow \mathrm{B} \rightarrow \mathrm{ABN}$, $\mathrm{A} \rightarrow \mathrm{B}$ and $\mathrm{B} \rightarrow \mathrm{ABN}$. We find that these patterns do indeed occur, and they are illustrated in Figures 11 and 12. However, they are not the only patterns this pulsar exhibits. In particular,

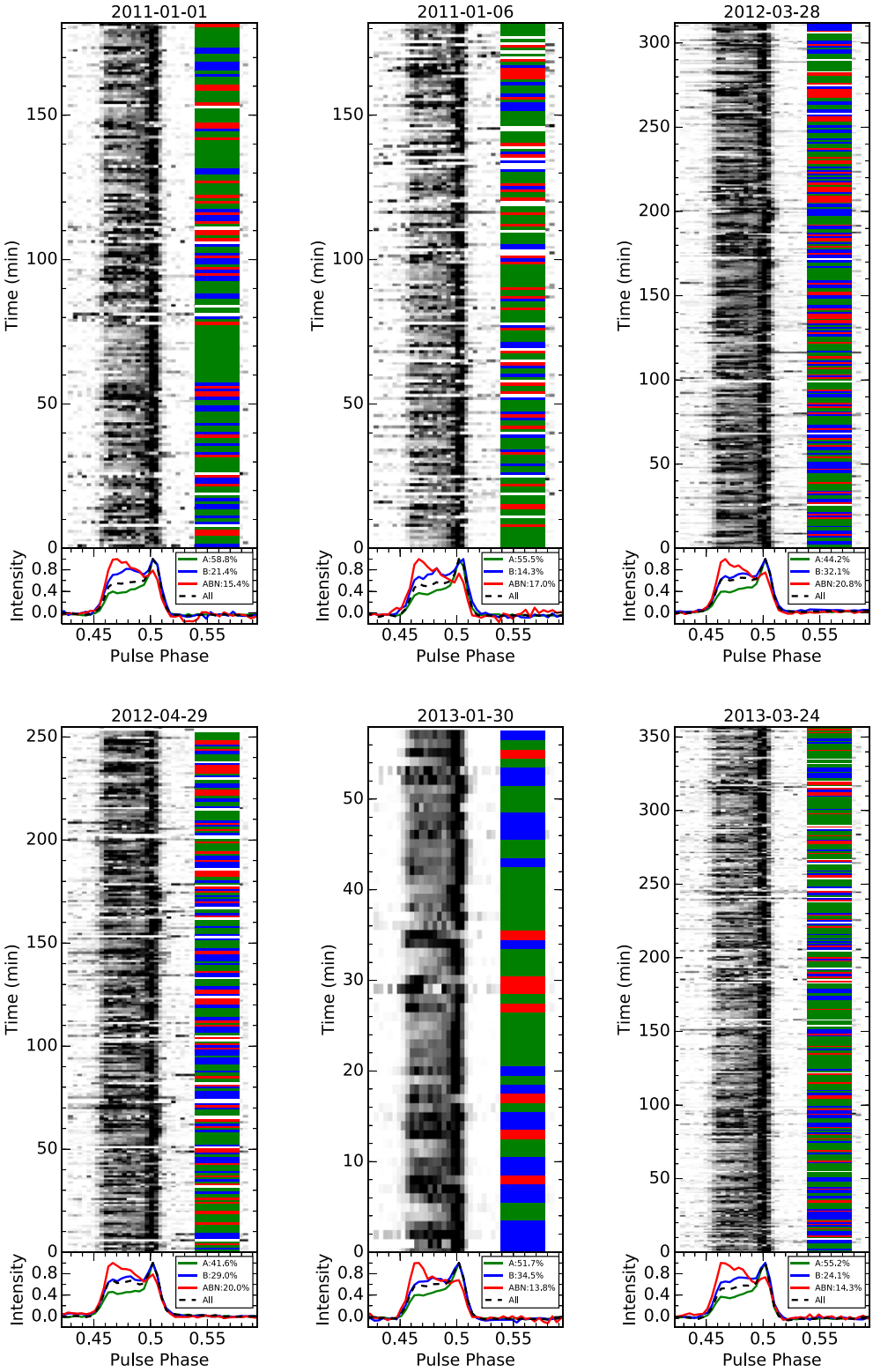

Figure 11. Stacked subintegrations of PSR B2319+60 for mode changes, each is integrated over 1 minute (upper panels). The gray-scale is linear in flux density from zero (white) to the maximum observed value (black). The observational date is labeled on the top. The separated profile modes A, B and ABN are indicated with green, blue and red bars, respectively. The remaining null pulses without emission are shown with white bars. The lower panels feature the averaged pulse profiles of mode A (green), B (blue) and ABN (red) obtained with the selected corresponding mode data. The dashed line represents the average pulse profile of all pulses. They are normalized by their respective peak intensities for comparison. The percentages of three modes are given at the upper right of the lower panels.

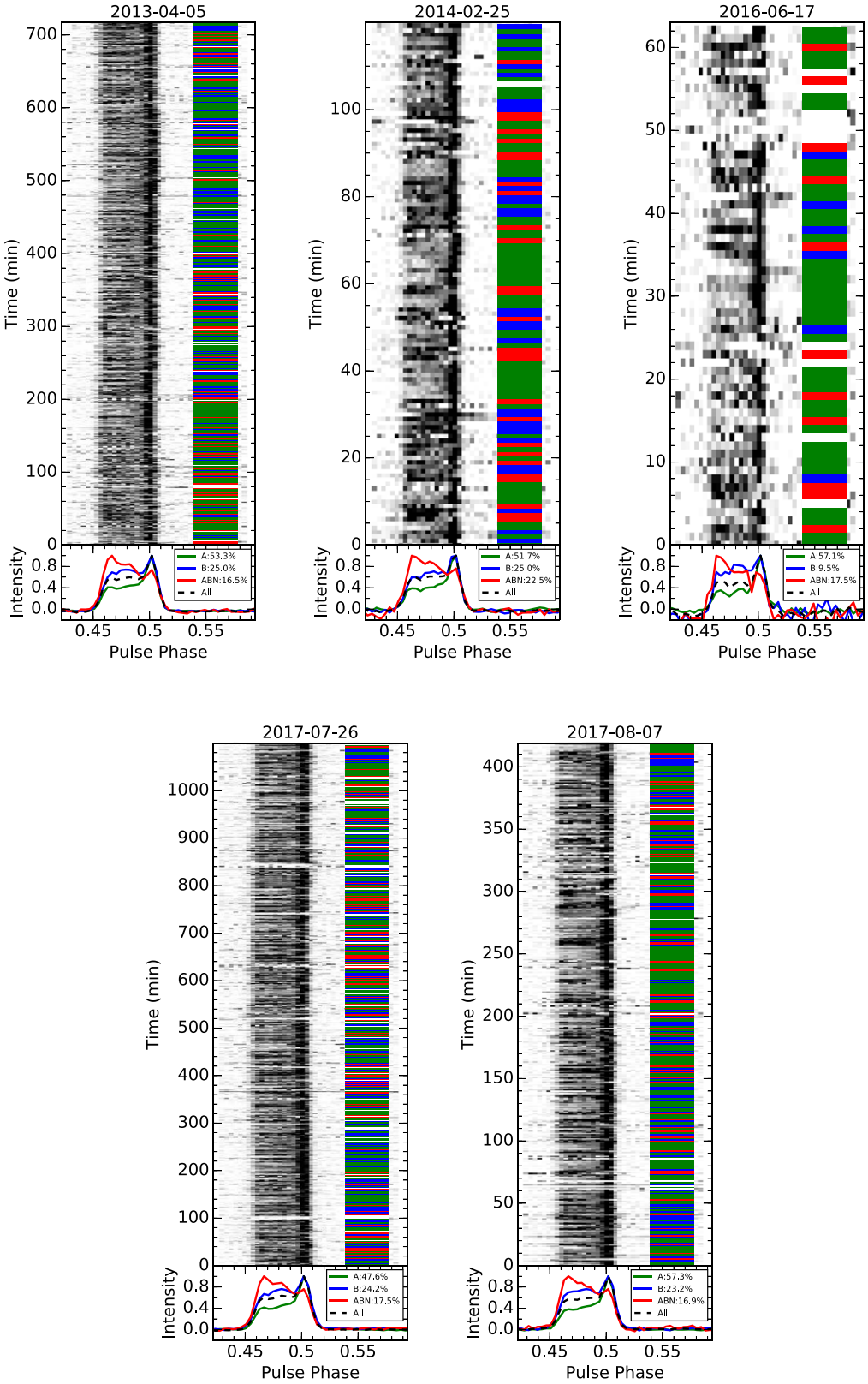

Figure 12. Stacked subintegrations and separated profile modes of PSR B2319+60 for five long observations as in Figure 11.

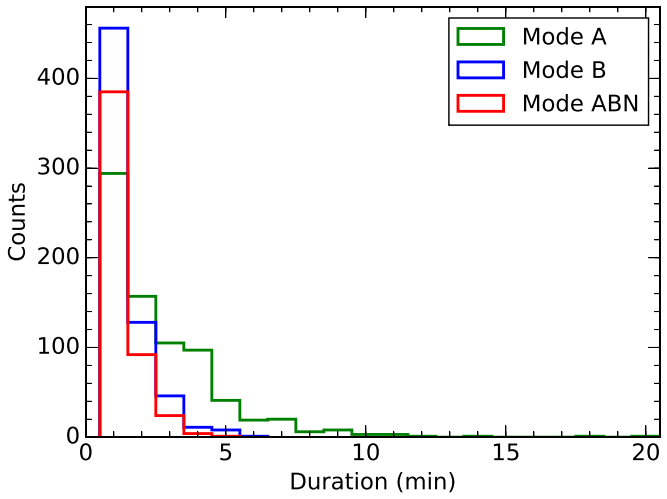

Figure 13. The observed histograms for the timescales of modes A (green), B (blue) and ABN (red).

there are frequent examples of the ABN mode being both preceded and followed by A and B modes.

5. Discussion

5.1. The Emission Geometry

The conal beam radii of the inner and outer cones corresponding to the two pairs of conal components in PSR B2319+60 are estimated based on a spherical geometric model described by the practice in Rankin (1993a, 1993b). Its respective inner and outer conal component pairs have half-power widths of 0.022 and 0.050, respectively, which are narrower than the measurement at 1 GHz given by Rankin (1993a, 1993b) due to the radius-to-frequency mapping effect (Cordes 1978). The radius of the conal emission beam is then determined to be $\rho_{\rm inner} = 6.^{\circ}9$ and $\rho_{\rm outer} = 9.^{\circ}7$ for the inner and outer cones, respectively. The steepest gradient point of the PPA is estimated from $\sin(\alpha)/\sin(\beta) = 7.72^{\circ}/^{\circ}$. The sightline which misses the core beam makes an oblique traverse through the outer emission conal zones (with $\beta/\rho_{\rm outer} \sim 0.6$) and encounters the inner cone tangentially (with $\beta/\rho_{\rm inner} \sim 0.9$), which confirms the qualitative interpretation of the star's double-conal emission geometry (Oster et al. 1977).

The phase-modulated subpulse drifting is associated with conal profiles with shallow PPA traverses. The pulse profile shape evolves with observing frequency, where the number of components decreases at high frequency (Rankin 1993b). The integrated profile of PSR B2319+60 exhibits four components at 408 MHz (Lyne & Manchester 1988), whereas the core component is not readily distinguished at high frequencies (Morris et al. 1981). Therefore, its profile has been placed in the relatively uncommon conal quadruple category at low

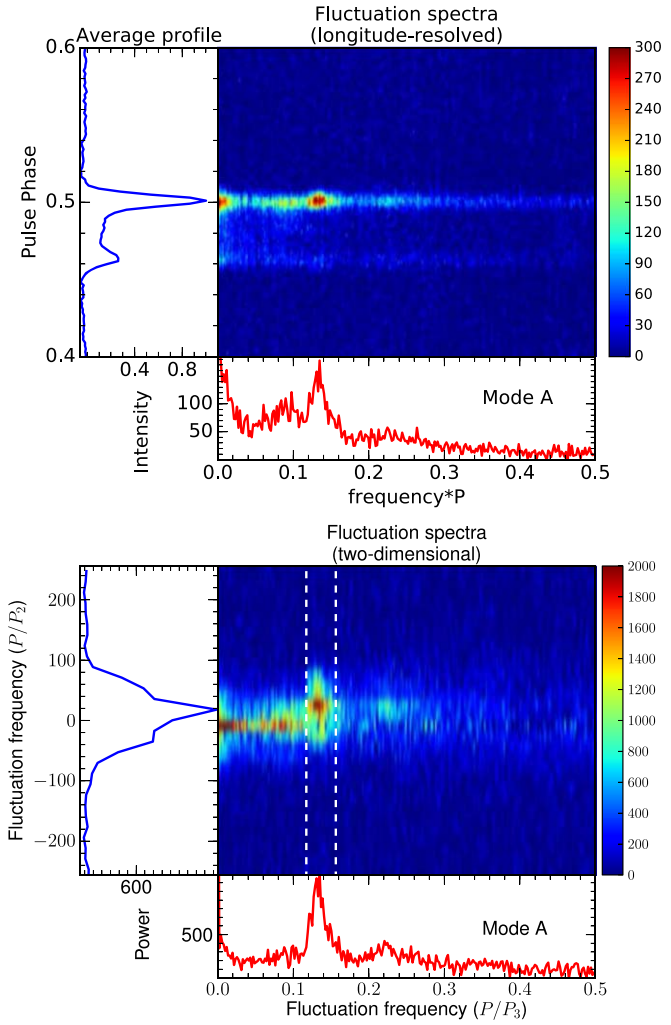

Figure 14. LRFS (upper panel) and 2DFS (lower panel) for PS corresponding to mode A, which show the drifting to be present only in the trailing component. The prominent drift feature is visible at $P_3 = 7.4 \pm 1.2P_1$ and $P_2 = 20.1 \pm 7.5$ deg.

frequency (Rankin 1993a, 1993b). Considering a scenario of narrow band emission, the high-frequency emission is assumed to be generated at a low altitude and vice versa, called radius-to-frequency mapping (Cordes 1978). As the line of sight sweeps across the inner and outer cones, the beam size shrinks at high frequency. As the line of sight approaches the edge of the cones, only a patchy beam located in the inner cone and two patchy beams in the outer cone are visible, which result in three components at high frequency. So, we conclude that the profile classification for PSR B2319+60 at 1.5 GHz is consistent with conal triple type.

Comparison with the average pulse profiles in the three primary modes suggests that the shapes are distinct while widths remain largely unchanged. Widths of pulse at 50% (W_{50}) and 10% (W_{10}) of peak height as well as the uncertainty estimated with the rms level of the baseline are shown in

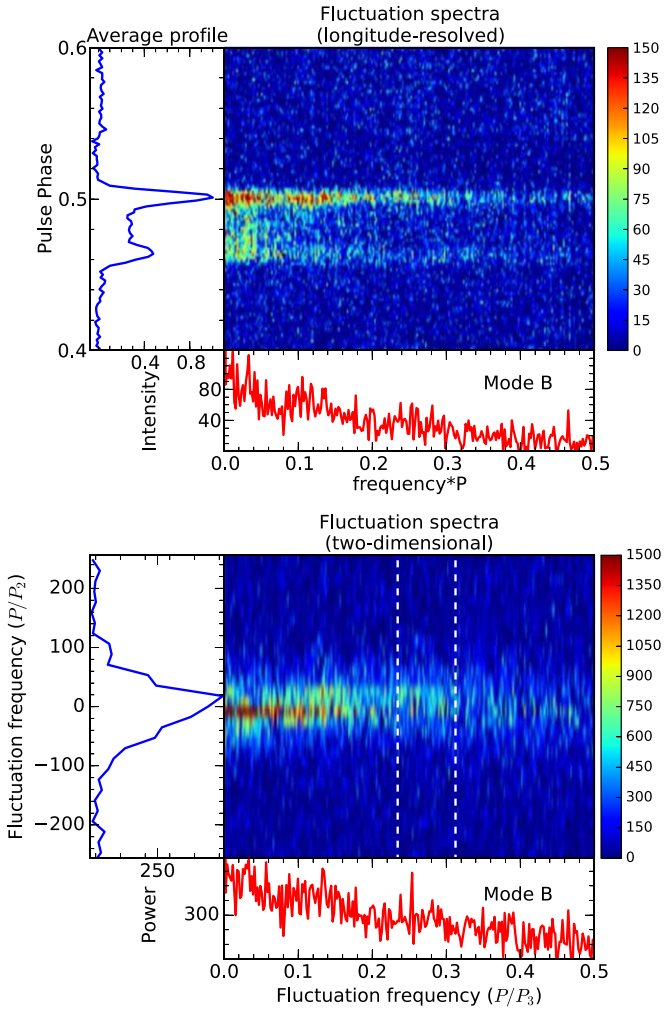

Figure 15. LRFS (upper panel) and 2DFS (lower panel) for PS corresponding to mode B. No significant modulation feature is detected.

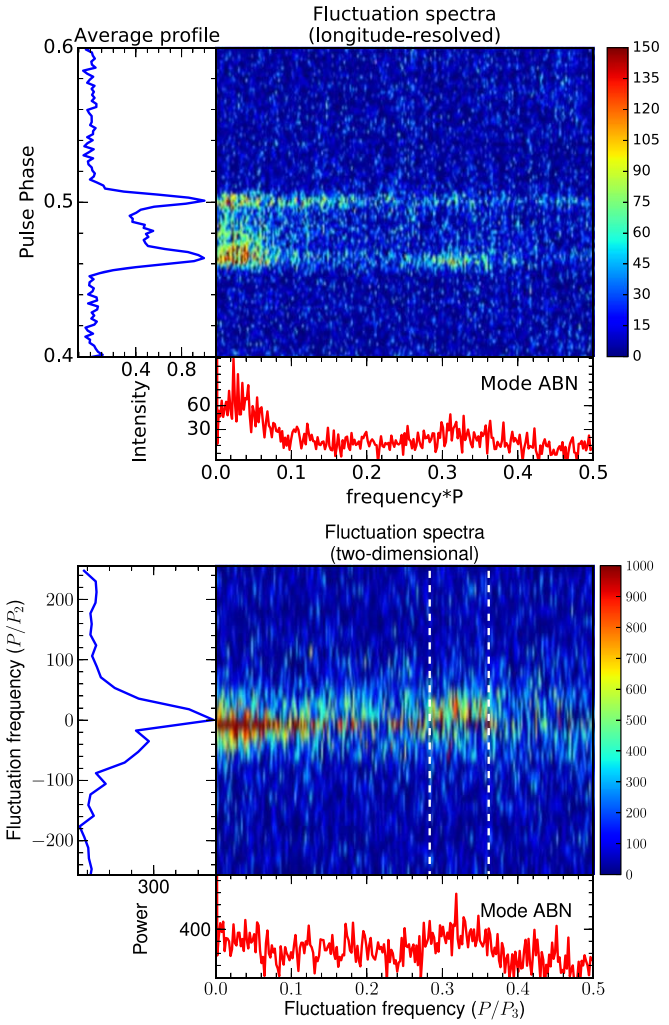

Figure 16. LRFS (upper panel) and 2DFS (lower panel) for PS corresponding to mode ABN. A widish structure can be discerned at $P_3 = 3.1 \pm 0.7P_1$ and $P_2 = 20.1 \pm 5.2P_1$ only in the leading component. In addition, a low-frequency excess, peaking at $P_3 = 40P_1$, is detected both in the leading and trailing components.

Table 2. This signifies that the emission regions in different modes are bounded by similar scales along the magnetic open field lines. Additionally, we have also carried out comparisons of the PPA traverse, and the linear and circular polarization across the pulsar profile for the three modes are plotted in Figure 17 (mode A in black solid line, mode B in blue dash–dotted line and mode ABN in green dashed line). The PPA traverses (top panel) are identical for the three modes with the same RVM fitting. Mode A seems to have slightly higher linear polarization toward the leading and central part of the profile but no discernible difference in circular polarization could be seen in the three modes, which could be associated with changes in plasma inhomogeneity (Melikidze et al. 2014). These analyses show that during the mode changing the emission region remains largely unaffected and the emission continues to arise from the same altitudes.

5.2. Association between Subpulse Drifting and Mode Changing

The presence of multiple drifting modes associated with different pulse profiles and periodic nulling feature in PSR B2319+60 provides a unique opportunity to further investigate the physical conditions in the pulsar magnetosphere. The radio emission originates at heights of a few hundred kilometers above the stellar surface which are dominated by dipolar magnetic field lines. The plasma that originated in the inner acceleration region leads to coherent curvature radio emission. The observed subbeams correspond to a number of sparks which circulate around the pulsar's magnetic axis due to the $\boldsymbol{E} \times \boldsymbol{B}$ which has been proposed in the framework of the

Table 2
List of the Drift Parameters During the Different Emission Modes of PSR B2319+60

Mode	% of Pulses	P_2 (deg)	P_3 (P_1)	W_{10} (deg)	W_{50} (deg)	S_{1556} (mJy)
A	41.58 (52.18)	20.1 ± 7.5	7.4 ± 1.2	22.5 ± 1.8	17.6 ± 1.8	13.85 ± 0.02
B	16.47 (23.85)	...	...	24.1 ± 3.7	18.6 ± 3.7	20.78 ± 0.12
ABN	14.89 (17.47)	20.1 ± 5.2	3.1 ± 0.7	25.3 ± 2.9	18.4 ± 2.9	11.23 ± 0.07
N	27.06 (6.50)	...	...	...	...	...

Note. The percentages of pulses for different modes obtained from the fold mode observations are presented in parentheses in the second column.

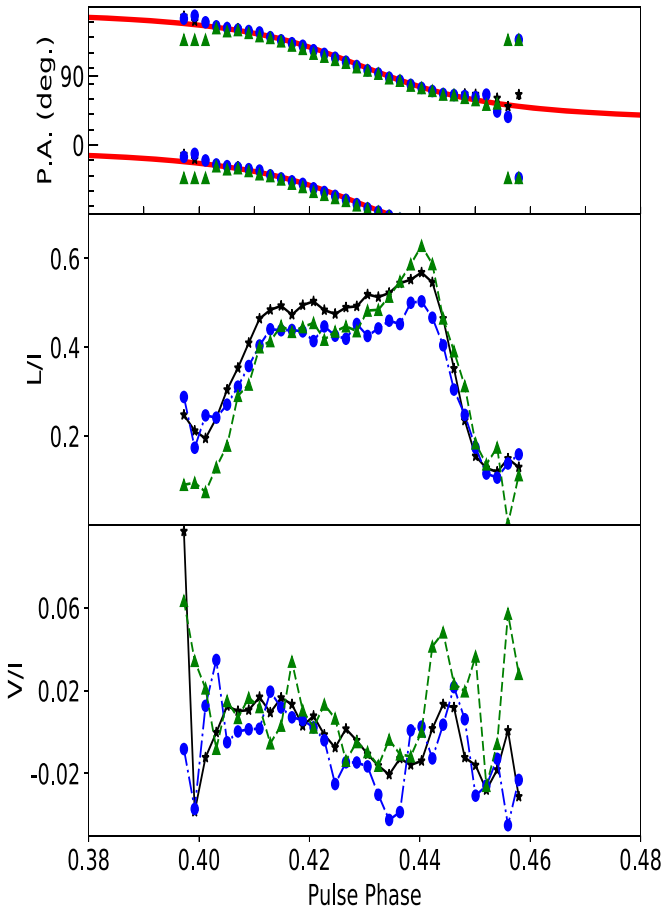

Figure 17. This figure displays the comparison of the polarization properties across the pulse window for the three emission modes A (in black stars), B (in blue circles) and ABN (in green triangles). The top window shows the PPA in the three modes with a realization of the RVM (red line), which accurately fits the PPA in the three modes. The middle window features the fractional linear polarization (L/I) at each pulse longitude. The bottom window plots the fractional circular polarization (V/I) at each pulse longitude.

rotating carousel model (Ruderman & Sutherland 1975). Then the observed subpulse drifting arises due to the individual subbeam gradually moving across the observer's line of sight at the observed drift rate. Therefore, the presence of two phase modulated subpulse drifting properties from PSR B2319+60 is useful to better understand the conditions in the inner acceleration region. The drifting periodicity can be estimated as $P_3 = d/\nu_d$, where d is the separation between two consecutive discharging sparks and ν_d is the drift velocity of the sparks. The separation between the sparks is approximately related to P_2 and the pulsar geometry. The emission geometries for different modes are similar as argued in the previous section. As reported earlier, modes A and ABN have similar P_2 values as shown in Table 2. This implies that the spacing between sparks and number of sparks both remains constant for different emission modes. Hence, the variation of P_3 values is attributed to the changes in ν_d. In the inner acceleration region, ν_d can be further expressed as $\nu_d = (\Delta E/B)c$, where ΔE is the change in electric field, B is the magnetic field and c is the speed of light. The change in magnetic field may be not considered at all since this will result in large scale reorientation of the current flow in the pulsar circuit (Spitkovsky 2011). Therefore, the change in P_3 is a direct indication that the ΔE in the gap is changing. According to Ruderman & Sutherland (1975), the sparking discharges take place due to pair production from γ-ray photons in the large electromagnetic fields. The variation of different pulse profiles may be attributed to the changes of ΔE as well. In this work the subpulse drifting features are restricted to the outer conal regions, which may indicate that the electric field in the outer cone is unstable.

The periodic-nulling and low-frequency amplitude modulation in mode ABN are presented in PSR B2319+60, which suggest that an external triggering mechanism could periodically affect the plasma flow in the pulsar magnetosphere. However, the origin of these phenomena is still not clear to us and requires more detailed modeling of the physical conditions in the inner acceleration gap.

6. Concluding Remarks

We have carried out detailed analyses of the polarimetric profile geometry and the single pulse dynamics in the drift mode changing pulsar B2319+60. Two distinct emission states and three different modes have been identified. The primary distinguishing feature among the different emission modes is the nature of profile mode changing. The LRFSs and 2DFSs corresponding to different emission modes are determined as

well. The fluctuation research of segregated modes suggests that PSR B2319+60 is dominated by the mode A phase modulation with a cycle of nearly seven periods for around 42% of time. Prominent drift bands are present only across the trailing component. Around 16% of the observing duration is identified as mode B, and no significant subpulse drifting feature is present. A third mode ABN is comprised of a second phase modulation mode with periodicity of three periods, and an amplitude modulation with periodicity of 40 periods. In addition to the three distinct emission modes, PSR B2319+60 also displays the presence of nulling throughout all the observations. The nulling is shown to exhibit quasi-periodicity with four pulse periods.

The radio emission in PSR B2319+60 is unique owing to the diversity of single pulse phenomena shown in the same system. The emission region remains constant in the three modes. We have explored the physical processes in the pulsar magnetosphere that can give rise to subpulse drifting, nulling and mode changing. The variations in subpulse drifting during mode changing are likely driven by the changes of ΔE in the inner acceleration gap during the sparking process. The periodic nulling and periodic amplitude modulation indicate that an additional triggering mechanism in the pulsar magnetosphere would be required to change the plasma generation process periodically.

Acknowledgments

We would like to thank the anonymous referee for providing constructive suggestions that improved the article. This work is partially supported by the National Natural Science Foundation of China (NSFC, Grant Nos. U1631106, U1838109, 12133004, 12041304 and 12041301) and the National SKA Program of China (2020SKA0120100). Z.G.W. is supported by the 2021 project Xinjiang Uygur Autonomous Region of China for Tianshan elites. J.L.C. is supported by the Natural Science Foundation of Shanxi Province (20210302123083) and the Scientific and Technological Innovation Programs of Higher Education Institutions in Shanxi (Grant No. 2021L470). H.W. is supported by the Scientific and Technological Innovation Programs of Higher Education Institutions in Shanxi(Grant No.2021L480). W.M.Y. is supported by the CAS Jianzhihua project. H.G.W. is supported by the 2018 project of Xinjiang Uygur Autonomous Region of China for flexibly fetching upscale talents. This work made use of the data from the Nanshan 25 m radio telescope, which is operated by Xinjiang Astronomical Observatories, Chinese Academy of Sciences. We thank the observers for setting up the observations.

ORCID iDs

Jian-Ling Chen https://orcid.org/0000-0003-4705-5255
Zhi-Gang Wen https://orcid.org/0000-0003-2991-7421
Vishal Gajjar https://orcid.org/0000-0002-8604-106X
Wen-Ming Yan https://orcid.org/0000-0002-7662-3875

References

Backer, D. C. 1970a, Natur, 227, 692
Backer, D. C. 1970b, Natur, 228, 1297
Backer, D. C. 1970c, Natur, 228, 42
Basu, R., & Mitra, D. 2018, MNRAS, 475, 5098
Cordes, J. M. 1978, ApJ, 222, 1006
Cordes, J. M., & Lazio, T. J. W. 2002, arXiv:astro-ph/0207156
Drake, F. D., & Craft, H. D. 1968, Natur, 220, 231
Edwards, R. T., & Stappers, B. W. 2002, A&A, 393, 733
Force, M. M., Demorest, P., & Rankin, J. M. 2015, MNRAS, 453, 4485
Gajjar, V., Joshi, B. C., & Kramer, M. 2012, MNRAS, 424, 1197
Gajjar, V., Joshi, B. C., & Wright, G. 2014, MNRAS, 439, 221
Herfindal, J. L., & Rankin, J. M. 2007, MNRAS, 380, 430
Hotan, A. W., van Straten, W., & Manchester, R. N. 2004, PASA, 21, 302
Lyne, A. G., & Manchester, R. N. 1988, MNRAS, 234, 477
Manchester, R. N., Hobbs, G. B., Teoh, A., & Hobbs, M. 2005, AJ, 129, 1993
Melikidze, G. I., Mitra, D., & Gil, J. 2014, ApJ, 794, 105
Mitra, D., & Li, X. H. 2004, A&A, 421, 215
Morris, D., Graham, D. A., Sieber, W., Bartel, N., & Thomasson, P. 1981, A&AS, 46, 421
Ng, C., Pandhi, A., Naidu, A., et al. 2020, MNRAS, 496, 2836
Oster, L., Hilton, D. A., & Sieber, W. 1977, A&A, 57, 323
Radhakrishnan, V., & Cooke, D. J. 1969, ApL, 3, 225
Rahaman, S. k. M., Basu, R., Mitra, D., & Melikidze, G. I. 2021, MNRAS, 500, 4139
Rankin, J. M. 1993a, ApJ, 405, 285
Rankin, J. M. 1993b, ApJS, 85, 145
Rankin, J. M., Wright, G. A. E., & Brown, A. M. 2013, MNRAS, 433, 445
Redman, S. L., Wright, G. A. E., & Rankin, J. M. 2005, MNRAS, 357, 859
Ruderman, M. A., & Sutherland, P. G. 1975, ApJ, 196, 51
Spitkovsky, A. 2011, ApSSP, 21, 139
Timokhin, A. N. 2010, MNRAS, 408, L41
van Straten, W., Demorest, P., & Oslowski, S. 2012, AR&T, 9, 237
van Straten, W., Manchester, R. N., Johnston, S., & Reynolds, J. E. 2010, PASA, 27, 104
Wang, N., Manchester, R. N., & Johnston, S. 2007, MNRAS, 377, 1383
Wang, N., Manchester, R. N., Zhang, J., et al. 2001, MNRAS, 328, 855
Weltevrede, P., Edwards, R. T., & Stappers, B. W. 2006, A&A, 445, 243
Weltevrede, P., Stappers, B. W., & Edwards, R. T. 2007, A&A, 469, 607
Wen, Z. G., Wang, N., Yan, W. M., et al. 2016a, Ap&SS, 361, 261
Wen, Z. G., Wang, N., Yuan, J. P., et al. 2016b, A&A, 592, A127
Wen, Z. G., Yan, W. M., Yuan, J. P., et al. 2020, ApJ, 904, 72
Wright, G. A. E., & Fowler, L. A. 1981, A&A, 101, 356